Icarus 321 (2019) 14–28

Contents lists available at ScienceDirect

Icarus

journal homepage: www.elsevier.com/locate/icarus

Mapping olivine abundance on asteroid (25143) Itokawa from Hayabusa/NIRS data

L. Nardi[*,a,d], E. Palomba[a,b], A. Longobardo[a,c], A. Galiano[a,e], F. Dirri[a]

[a] INAF-IAPS, Via Fosso del Cavaliere 100, Roma 00133, Italy
[b] ASI-SSDC, via del Politecnico, Roma 00133, Italy
[c] Università Parthenope, Dist. Centro Direzionale Isola C4, 80143, Italy
[d] La Sapienza Università di Roma, Piazzale Aldo Moro 5, Roma 00185, Italy
[e] Università degli Studi di Roma Tor Vergata, Via Orazio Raimondo 18, Roma 00173, Italy

ARTICLE INFO

Keywords:
Asteroid Itokawa
Asteroid surfaces
Infrared observations
Spectroscopy
Mineralogy

ABSTRACT

Olivine is one of the main abundant mineral in the Solar System, and the determination of its abundance on a surface may give fundamental information about its evolution. The study of surface distribution of olivine on asteroid (25143) Itokawa through near-Infrared reflectance spectroscopy is a difficult goal because olivine and pyroxene bands centred at 1 μm and 2 μm are not entirely included in Hayabusa/NIRS' spectral range. In this work, the retrieval of olivine abundance has been performed by applying two different methods: the first one uses some spectral indices to retrieve olivine abundance, whilst the second one consists of the application of the Hapke's theory in order to create synthetic spectra aimed at fitting a selection of NIRS' spectra. The analysis performed with the first method brought to an approximately homogeneous distribution of olivine content (60 ± 15% on average) on Itokawa's surface, with the exception of Sagamihara region, which has a slightly (up to 10%) lower olivine content. The second method brought to an average 60 ± 7.5% olivine content within 5 selected spectra, with the same reduction found in the spectrum from the Sagamihara region. All these values are in agreement with literature values on this topic, especially with the ones retrieved from particles sampled in Muses Sea by the Hayabusa probe.

1. Introduction

In 2005 JAXA's Hayabusa spacecraft visited near-Earth asteroid (25143) Itokawa, bringing some surface samples back to Earth in 2010. The spacecraft was equipped with four main scientific instruments: (1) Light Detection And Ranging instrument (LIDAR; Mukai et al., 2002), (2) Asteroid Multi-band Imaging Camera (AMICA; Nakamura et al., 2001), (3) X-ray Fluorescence Spectrometer (XRS; Okada et al., 2000), and (4) Near Infra-Red Spectrometer (NIRS; Abe et al., 2004).

The shape of Itokawa is generally compared to that of a sea otter (Enhydra lutris) and therefore the asteroid is commonly divided into two main regions designated as "head" and "body" respectively corresponding to the smaller and larger section of the asteroid, connected by a narrower region named "neck". Fujiwara et al. (2006) suggested that the asteroid has a rubble pile structure, a self-gravitating agglomerate of debris with dimensions up to 50 m. Saito et al. (2006) distinguished essentially two types of terrain on the surface of Itokawa: a rough one (80% of the surface) that is rich in boulders, and a smooth one (remaining 20% of the surface), poor in boulders.

Itokawa is a near-Earth asteroid of the Apollo group and was discovered on 26th September 1998 by the LINEAR program. Itokawa rotates quite quickly in the retrograde direction, with a 12.1 hours period and axis almost perpendicular to the ecliptic plane (Fujiwara et al., 2006). Its size is 0.535 × 0.294 × 0.209 (± 0.001) km^3 (Saito et al., 2006) and its mass is (3.51 ± 0.02) × 10^{10} kg (Fujiwara et al., 2006). Before Hayabusa mission results, observations from Earth (Binzel et al., 2001; Abell et al., 2007) in visible and near infrared were used to estimate the mineralogy of Itokawa. Binzel et al. (2001), using asteroid observation from NASA's IRTF in March 2001 inferred that the composition of Itokawa was similar to that of an LL chondrite, according to olivine/pyroxene content, but with a significant reddening of the bands due to the effects of space weathering on the surface. Abell et al. (2007) confirmed that Itokawa mineralogy is dominated by olivine and pyroxene, founding out that the latter were richer in iron ($Fs_{43 \pm 5}$) than average ordinary chondrites (Fs_{14-26}). From these observations, the

* Corresponding author at: INAF-IAPS, Via Fosso del Cavaliere 100, Roma 00133, Italy.
E-mail address: luca.nardi@iaps.inaf.it (L. Nardi).

https://doi.org/10.1016/j.icarus.2018.10.035
Received 26 May 2018; Received in revised form 13 August 2018; Accepted 30 October 2018
Available online 01 November 2018
0019-1035/

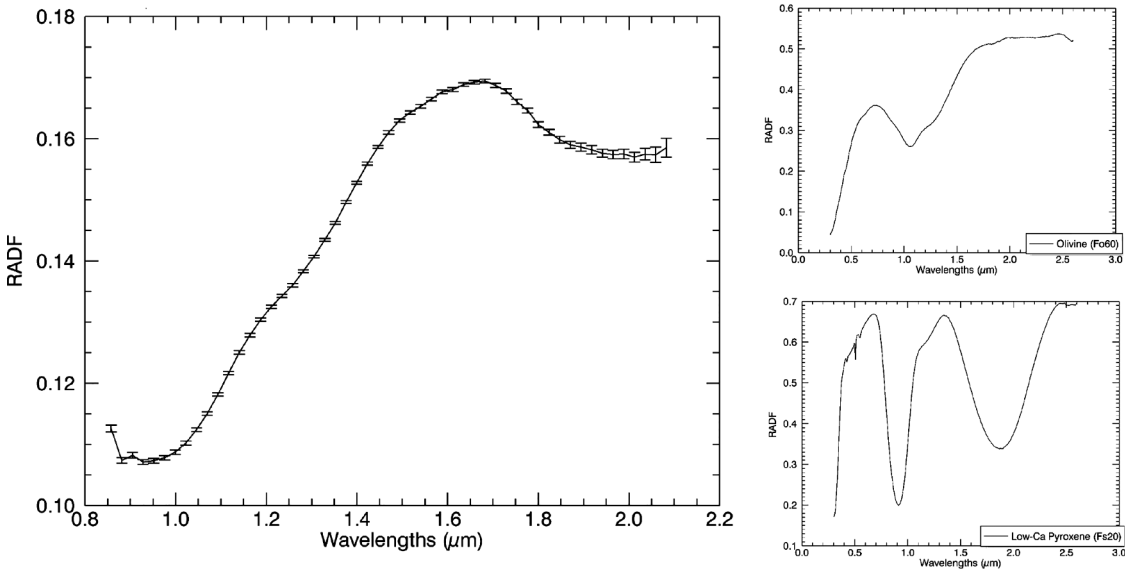

Fig. 1. A typical spectrum of Itokawa taken by NIRS. Error bars are given as the standard deviation. The spectrum has been smoothed with a boxcar average filter with a width of 5 points in order to improve SNR. Small plots on the right report an example of olivine spectrum (Fo_{60}, top right) and of low-Ca pyroxene (Fs_{20}, bottom right), obtained from the RELAB database at 0° emission angle and 30° incidence angle.

average value of the ratio of olivine to pyroxene is 75:25 ± 5 on Itokawa.

The NIRS wavelength range does not completely include the absorption bands at 1 and 2 μm. Using a constant continuum for the band at 2 μm and the shortest NIRS wavelength as a continuum shoulder for the band at 1 μm, Abe et al. (2006) found out that NIRS data seem to define a mineralogy rich in olivine, similar to LL5 or LL6 chondrites; in particular, band ratios suggest that the olivine abundance with respect to pyroxene is included between 70% and 80% for Itokawa. Bhatt et al. (2015) found out that on Itokawa is expected a Fa content between 25% and 30% and Fs between 21% and 25%. The two samplings took place on 19th and 25th November 2005 in the Muses Sea region. Oxygen isotopic ratios, measured by Yurimoto et al. (2011), allow to define Itokawa as a potential source of LL4-LL6 chondrites. Mikouchi et al. (2014) used X-ray analysis techniques to verify that the analysed samples were olivine and plagioclase compounds with Ca and chromite phosphate traces, whilst the presence of pyroxene was not seen. In particular, olivine was of the type Fo_{70-73} and plagioclase of the type $An_{13-10}Or_{5-7}$, consistent with those of the LL chondrites. Tsuchiyama et al. (2014) analysed 48 Itokawa regolith particles through synchrotron microtomography and compare their microstructure with the microstructure of some ordinary chondrites, finding that Itokawa particles are consistent to LL (both LL5 and LL6) chondrites in terms not only of elemental (Nakamura et al., 2011) and oxygen isotopic compositions (Yurimoto et al., 2011), but also of their microstructure. Therefore, the analysis of Hayabusa's samples confirmed the LL-like composition of Itokawa, confirming the ground-based and probe observations.

This work is aimed at finding a method for olivine abundance retrieval using spectroscopic techniques on NIRS' data. Spectroscopy in the near-Infrared spectral range is a powerful method in order to obtain information from planetary surfaces, such as mineralogy, composition, and grain size distribution (Hapke, 2012). Two approaches have been used in this work: the first one uses some spectral indices to retrieve olivine abundance, whilst the second one consists of the application of the Hapke's theory in order to create synthetic spectra aimed at fitting a selection of NIRS' spectra

In the second section of this work datasets are described, whilst the third section introduces and describes the two methods used for their analysis. The fourth section shows the results obtained by applying these two methods, and the fifth and sixth sections are respectively discussion and conclusions. Both methods and results section treat separately the spectral indices and synthetic spectra methods.

2. Data

We considered Hayabusa/NIRS data sets calibrated in radiance factor I/F by Abe et al. (2011), and available on NASA's Planetary Data System; they include 111,226 I/F spectra returned by NIRS instrument. The data cover the Itokawa encounter phase, from 31th August to 24th November 2005. For the sake of simplicity, hereafter we will use the terms "radiance factor" and "reflectance" as synonyms.

The NIRS effective spectral range is comprised between 0.86 and 2.1 μm with a spectral sampling resolution of 23.6 nm (53 effective channels; Abe et al., 2011). Its field of view is 0.1° × 0.1°, corresponding to a footprint size between 6 and 90 m^2 during observational phases. During these phases, observation phase angles varied between 0° and 38°.

NIRS data are organised into four sets, according to the following mission phases: *Approaching Phase* (AP, between 50 km and 20 km from Itokawa), *Gate-Position Phase* (GP, between 20 km and 8 km from Itokawa), *Home-Position Phase* (HP, around 7 km from Itokawa), and *Descent and Touchdown phase* (TD, descent for surface sampling). Itokawa is 535 × 294 × 209 (± 1) m^3 (Fujiwara et al., 2006), so AP and GP spectra were taken too far from the target to resolve surface details, and therefore their spectra have not been considered in this work. Home Position was the main observational phase, so its data were the most reliable and useful ones, whilst TD had the advantage to have footprints at a higher spatial resolution. Footprint size was up to 17 × 17 m^2 and down to 6 × 6 m^2 in these phases.

The data set selected and used in this work includes 31,362 HP, and 17,397 TD spectra.

3. Methods

The study of surface distribution of olivine on Itokawa is a difficult goal because olivine and pyroxene bands centred at 1 μm and 2 μm are not entirely included in NIRS' spectral range (Fig. 1). This would not have been an issue if the two bands had been symmetric, but this is not the case, since olivine band at 1 μm is strongly asymmetric (Clark, 1999). Therefore, we applied two methods to detect olivine and retrieve its abundance.

The first one, described in Section 3.1, uses some spectral indices, that are combinations of reflectance values at some specific wavelengths which have been found out to be empirically related to olivine abundance. The second one, treated in Section 3.2, consists of the application of the Hapke's theory in order to create synthetic spectra aimed at fitting a selection of NIRS' spectra.

3.1. Spectral indices

Many spectral indices capable to retrieve olivine abundance from a reflectance spectrum have been defined (Cloutis et al., 1986; Palomba et al., 2015; Poulet et al., 2007), but most of them need a spectral range larger than the NIRS one (0.86–2.1 μm).

Cloutis et al. (1986) suggested that the Band Area Ratio (BAR) and the Band I centre are the best olivine indicators. These parameters cannot be defined on NIRS spectra because of the incompleteness of the two bands. In addition, the computation of Band II centre is complicated by the reduction of SNR at the longest wavelengths of NIRS spectral range.

Thus, it was necessary to use or define other spectral indices. Here, three indices are discussed and compared. The Forsterite Index, the Modified BAR*, and the Px Index.

All these indices are essentially given by reflectance ratios or combination of reflectance ratios. It is a common assumption that asteroid reflectance is given by the products of two terms, i.e. a wavelength-independent disk function depending on local topography (i.e. incidence and emission angle) and a phase function, depending on the phase angle (e.g., Schroeder et al., 2013; Longobardo et al., 2017a; Ciarniello et al., 2015). Therefore, spectral indices defined in this work are expected to depend only on phase angle, and not on the other two observation and illumination angles. On the other hand, the phase function behaviour is mainly driven by the reflectance level, and since outside the bands Itokawa spectral reflectance is almost constant, we could assume a phase function constant over the NIRS spectral range. This assumption is justified on findings on other minor bodies, such as Vesta (Longobardo et al., 2014), 67P/Churyumov-Gerasimenko (Longobardo et al., 2017a) and Ceres (Longobardo et al., 2017b). Therefore, a photometric correction of spectra is not needed and is not applied. In principle, the Forsterite Index may jeopardise this assumption because it uses an internal-to-band reflectance ($R_{1.01}$ in Eq. (1)), but its influence on the value of the parameter can be neglected since it is weighted with the smallest coefficient. This has been already verified by Palomba et al. (2015).

Forsterite Index. Poulet et al. (2007) defined a Forsterite and a Fayalite Index (hereafter FORx and FAYx, respectively), respectively diagnostic for the forsteritic and the fayalitic component of olivine:

$$FORx = \frac{0.5R_{1.54} + 0.5R_{1.56}}{0.1R_{1.01} + 0.2R_{1.21} + 0.7R_{1.36}} \quad (1)$$

$$FAYx = \frac{0.5R_{1.69} + 0.5R_{1.70}}{0.1R_{1.01} + 0.1R_{1.21} + 0.4R_{1.36} + 0.4R_{1.50}} \quad (2)$$

where R_λ is the reflectance at the wavelength λ (in μm).

Poulet et al. (2007) fixed the detection threshold at 1.04 and 1.02 for FORx and FAYx, respectively. However, these indices are affected also by other properties, such as grain size, presence of crystalline ferric oxides, or composition of the mixture. Ody et al. (2012), found that the FORx preferentially detects small olivine grain size and/or low abundance of olivine, whilst the FAYx is more sensitive to olivine with larger grains (i.e. more than 100 μm) and/or high olivine abundance.

Palomba et al. (2015) found that FORx and FAYx are strongly influenced by grain size only when the diameter of the particles is less than 75 μm, but FAYx is more affected by granulometry than FORx. On Itokawa, a great olivine abundance is expected, so FAYx would be a better choice. On the other hand, the lack of grain size information makes the FORx more suitable, due to its higher stability with grain size.

Px Index. Cloutis et al. (1986) analysed different spectral indices capable of retrieving olivine or pyroxene abundance. Almost all of them require the knowledge of reflectance at wavelengths that are outside of the NIRS spectral range. The only suitable index is the ratio of the reflectance at 1.4 μm to that at 1.9 μm, which will be referred to simply as Px Index. This index is related to pyroxene abundance, but it is possible to use it as an olivine index by assuming that the olivine and pyroxene abundances are complementary. This should not be a too strong assumption, since olivine and pyroxene are the main components of type S asteroids (Burbine, 2017).

Cloutis et al. (1986) found that this index increases with pyroxene abundance, with no systematic grain size dispersion for a pyroxene content lower than 80%. This can be applied to our case since, as previously said, for Itokawa a large olivine content with respect to pyroxene is expected.

*Modified BAR**. The BAR* is a variant of the Band Area Ratio (BAR), defined by Cloutis et al. (1986). Whereas BAR is the ratio between the band areas of pyroxene Band II and Band I (the bands centred at 2 μm and 1 μm, respectively), BAR* is defined as Band IIa/Band Ia. Band IIa is defined as the area between the spectrum and a straight horizontal line between Band II left shoulder (that is, the maximum reflectance between 1.4 and 1.7 μm) and Band II minimum, and Band Ia as Band I area times $R_{0.7}/R_{1.4}$.

Nevertheless, the BAR* definition is not applicable to the NIRS spectral range, neither. Therefore, a modified version has been defined as follows (Fig. 2):

$$BAR^*mod = \frac{R_{1.4}\ Band\ IIb}{R_{0.8}\ Band\ Ib} \quad (3)$$

where $R_{0.8}$ is the reflectance at the lowest NIRS wavelengths (which is 0.8578 μm), Band Ib is defined as the area between the spectrum and the continuum (in turn defined as the straight line starting from $R_{0.8}$ and tangent to the spectrum), Band IIb the area from the left shoulder of Band II and the last wavelength available for NIRS, that is 2.0829 μm. We considered the latter instead of the band minimum, because the larger noise level at these wavelengths makes the minimum definition ambiguous.

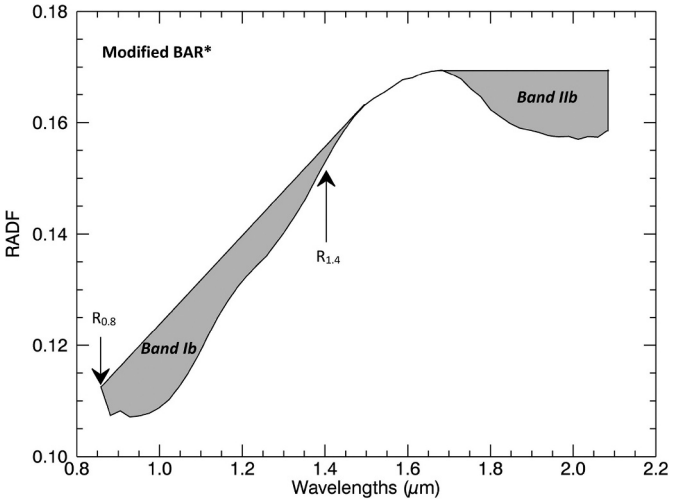

Fig. 2. An illustration that describes the parameters used for the Modified BAR*.

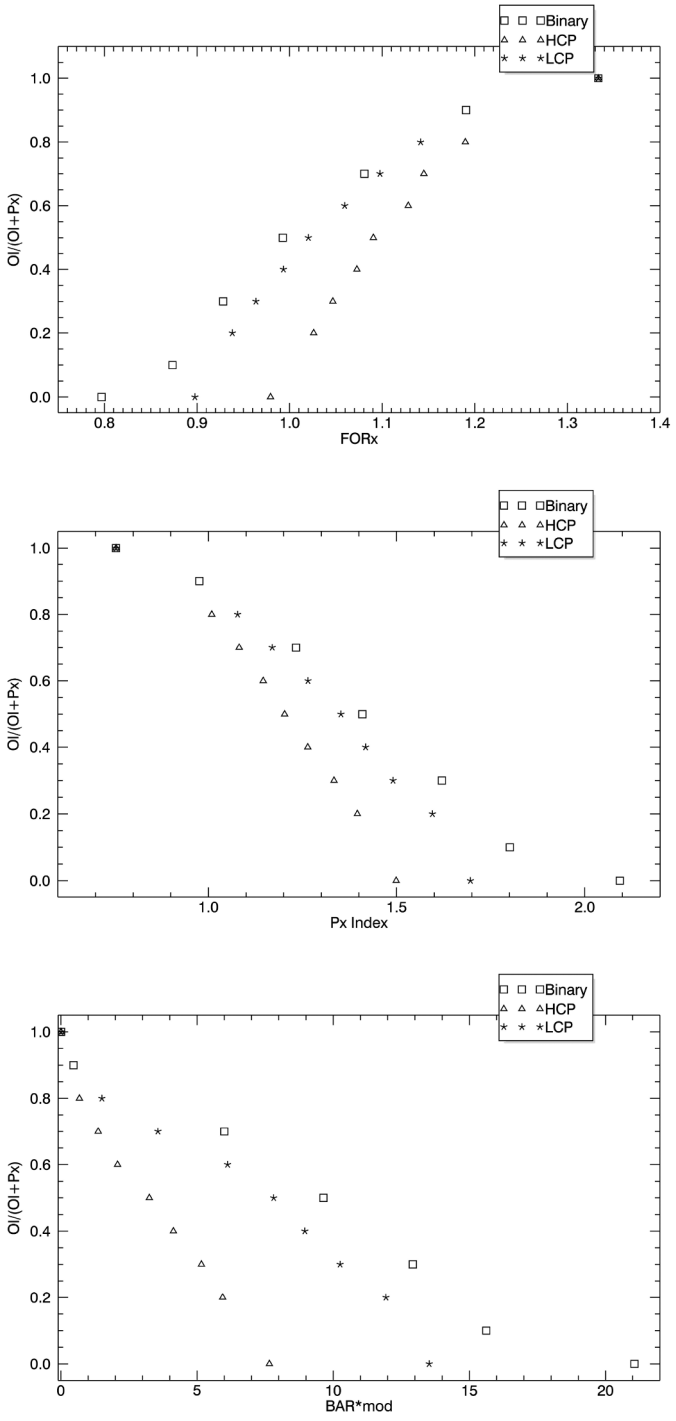

Fig. 3. Forsterite Index (top), Px Index (middle), and Modified BAR* (bottom) applied to binary (squares), HCP ternary (triangles), and LCP ternary (stars) silicate compounds. Error bars are not plotted since they are too small to be easily visible on this scale (see Table 1 for values).

3.1.1. Calibration of spectral indices

Olivine abundance calibration of spectral indices has been performed using spectra of binary and ternary mixtures available on the RELAB database (obtained at the Smithsonian Insitute at 30° incidence angle, 0° emission angle, and 30° phase angle).

- Binary mixtures consisted of hypersthene and forsterite (Fo_{90}).
- High-Ca ternary ones consisted of Fo_{90}, hypersthene (low-Ca pyroxene) and augite (high-Ca pyroxene) with a hypersthene/augite ratio equal to 1.
- Low-Ca ternary ones were similar to High-Ca but with hypersthene/augite ratio equal to 5.66.

Hereafter, binary mixtures will be referred to as “binaries”, while high-Ca and low-Ca ternary ones will be referred to as “HCPs” and “LCPs”. Grain size of pure forsterite and hypersthene samples was 0–45 μm, whilst the mixtures grain size was 0–38 μm. We calculated FORx, Px Index and Modified BAR* for the described binary and ternary mixtures. Results are reported in Table 1 and plotted in Fig. 3. The errors on the indices have been calculated with the error propagation formula using the errors on RELAB spectra.

Spectral indices were also calibrated by considering meteorite spectra of different grain-sized samples of ordinary chondrites available on RELAB database (Table 2, calibration results are reported in Section 4.1). All these spectra were obtained with the observation geometry at 30° incidence angle, 0° emission angle and 30° phase angle.

After calibration phase, these indices have been used to retrieve Itokawa’s olivine abundance distribution from NIRS’ spectra. Results will be shown in Section 4.

3.2. Synthetic spectra method

A more analytical approach uses the Hapke’s modelling (Hapke, 2012) in order to create synthetic spectra aimed at fitting NIRS ones. Hapke’s Theory is a widely used radiative transfer model that is capable to describe the behaviour of light scattered from a planetary surface. The method is firstly applied to some pyroxene mixtures and to a spectrum of Alta’ameem ordinary chondrite in order to test its accuracy, in particular using NIRS’ spectral range. Then, it is applied to a selection of NIRS spectra.

The method can be summarised in the following steps:

1. A number of reflectance spectra of mineral endmembers are selected and their optical constants retrieved by a numerical method.
2. The retrieved optical constants are used to create a single scattering albedo spectrum at the desired grain size for each endmember, by means of the Hapke’s modelling (Hapke, 2012).
3. Reflectance spectra of mixtures are obtained by mixing single scattering albedos from different endmembers.
4. Varying grain size in the second step and mass fractions in the third step, it is possible to search for the model spectrum which best fits the given one.

3.2.1. Optical constants

Considering a constant real part of the index of refraction n, which is an acceptable assumption in the Visible and near-Infrared region (Carli et al., 2016), the extinction coefficient k is calculated as in Roush (2005), that is to say at each wavelength an initial estimate of k is used to calculate the model reflectance and then k is iteratively adjusted until the difference between the model and measured reflectance is less than a given tolerance (here chosen as 10^{-5} in order to stay inside the average error values given in NIRS data from Abe et al. (2011).

The input reflectance data files for the endmembers have been taken from the RELAB database and their n values have been estimated as an average between the refraction indices of their component minerals, weighted with their mass fractions. A more accurate value for n could be obtained by using the equations by Lucey et al. (1998), but a negligible difference (up to 1% of n) is obtained in calculating n in the two ways. In addition, the equations by Lucey et al. (1998) need the Mg/(Mg + Fe) ratio, which for some endmembers is not known because of the lack of information in their RELAB label.

The input grain size has been estimated as the mean size of the sieve fraction. n and k should in principle be independent from grain size, but practically a wrong grain size input to Hapke’s equations strongly affects the resulting k spectrum. Indeed, a reflectance spectrum has to vary if grain size varies, because smaller particles are more reflective

Table 1
Spectral indices values for RELAB silicate compounds.

Mixture	%Ol	FORx	Px Index	BAR*mod	RELAB reference
binary	0	0.80 ± 0.01	2.09 ± 0.04	21.0 ± 0.5	AG-TJM-009/C1AG09
binary	10	0.87 ± 0.01	1.80 ± 0.03	15.6 ± 0.5	AG-TJM-017/C1AG17
binary	30	0.93 ± 0.01	1.62 ± 0.02	12.9 ± 0.3	AG-TJM-018/C1AG18
binary	50	0.99 ± 0.01	1.41 ± 0.01	9.6 ± 0.2	AG-TJM-019/C1AG19
binary	70	1.08 ± 0.01	1.23 ± 0.01	6.0 ± 0.1	AG-TJM-014/C1AG14
binary	90	1.19 ± 0.01	0.98 ± 0.01	0.4 ± 0.1	AG-TJM-020/C1AG20
binary	100	1.33 ± 0.02	0.76 ± 0.02	0.0 ± 0.1	AG-TJM-008/C1AG08
HCP	0	0.98 ± 0.01	1.50 ± 0.01	7.7 ± 0.2	AG-TJM-013/C1AG13
HCP	20	1.03 ± 0.01	1.40 ± 0.01	5.9 ± 0.1	AG-TJM-035/C1AG35
HCP	30	1.05 ± 0.01	1.33 ± 0.01	5.2 ± 0.1	AG-TJM-036/C1AG36
HCP	40	1.07 ± 0.01	1.26 ± 0.01	4.1 ± 0.1	AG-TJM-037/C1AG37
HCP	50	1.09 ± 0.01	1.20 ± 0.01	3.3 ± 0.1	AG-TJM-038/C1AG38
HCP	60	1.13 ± 0.01	1.15 ± 0.02	2.1 ± 0.1	AG-TJM-039/C1AG39
HCP	70	1.15 ± 0.01	1.08 ± 0.01	1.4 ± 0.1	AG-TJM-040/C1AG40
HCP	80	1.19 ± 0.01	1.01 ± 0.01	0.7 ± 0.1	AG-TJM-041/C1AG41
HCP	100	1.33 ± 0.02	0.76 ± 0.02	0.0 ± 0.1	AG-TJM-008/C1AG08
LCP	0	0.90 ± 0.01	1.70 ± 0.02	13.5 ± 0.3	AG-TJM-012/C1AG12
LCP	20	0.94 ± 0.01	1.60 ± 0.02	11.9 ± 0.3	AG-TJM-021/C1AG21
LCP	30	0.96 ± 0.01	1.49 ± 0.01	10.2 ± 0.2	AG-TJM-022/C1AG22
LCP	40	0.99 ± 0.01	1.42 ± 0.01	9.0 ± 0.2	AG-TJM-015/C1AG15
LCP	50	1.02 ± 0.01	1.35 ± 0.01	7.8 ± 0.2	AG-TJM-023/C1AG23
LCP	60	1.06 ± 0.01	1.27 ± 0.01	6.1 ± 0.1	AG-TJM-024/C1AG24
LCP	70	1.10 ± 0.01	1.17 ± 0.01	3.6 ± 0.1	AG-TJM-025/C1AG25
LCP	80	1.14 ± 0.01	1.01 ± 0.01	1.5 ± 0.1	AG-TJM-026/C1AG26
LCP	100	1.33 ± 0.02	0.76 ± 0.02	0.0 ± 0.1	AG-TJM-008/C1AG08

than larger ones (Hapke, 2012). The consequence is that a given reflectance spectrum can be obtained by increasing grain size or reducing absorption. It is possible to use other values for input grain size, assuming different size distribution in the samples, but here the mean size of the sieve is assumed, since it proved to be satisfactory during test phases (that will be discussed in the following).

3.2.2. Single scattering albedo

In order to create a synthetic reflectance spectrum, it is necessary to calculate the single scattering albedos of its components. The equation used are the ones obtained through the Equivalent Slab Model in Hapke (2012) and in Hapke (1981), which treats the particle as a slab with thickness equal to the particle diameter.

$$\alpha = \frac{4\pi k}{\lambda} \tag{4}$$

$$R(0) = \frac{(n-1)^2 + k^2}{(n+1)^2 + k^2} \tag{5}$$

$$S_E = 0.0587 + 0.8543R(0) + 0.0870R(0)^2 \tag{6}$$

$$S_I = 1 - \frac{1}{n^2}(0.9413 - 0.8543R(0) - 0.0870R(0)^2) \tag{7}$$

$$\langle D\rangle = \frac{2}{3}[n^2 - \frac{1}{n}(n^2-1)^{3/2}]D \tag{8}$$

$$D_e = \frac{1-S_E}{1-S_I}\langle D\rangle \tag{9}$$

$$Q_S = 1/(1+\alpha D_e) \tag{10}$$

$$w_i = Q_S \tag{11}$$

where α is the absorption coefficient, λ is the wavelength, $R(0)$ is the normal specular reflection coefficient, S_E and S_I are the surface reflectivity respectively from outside and from inside the grain, D is the grain diameter $\langle D\rangle$ is the average distance travelled by all rays during a single transit of the particle, D_e is an effective particle size, Q_S is the scattering efficiency, and finally w_i is the single scattering albedo for the ith component. More details on these equations can be found in Hapke (2012).

3.2.3. Synthetic spectra

Once the single scattering albedo for every endmember is computed, they are mixed using:

$$w = \frac{\sum_j \frac{M_j}{\rho_j d_j} w_j}{\sum_j \frac{M_j}{\rho_j d_j}} \tag{12}$$

$$p(g) = 1 + b\cos g + c[1.5\cos^2 g - 0.5] \tag{13}$$

$$\gamma = \sqrt{1-w}\, r_0 = \frac{1-\gamma}{1+\gamma} \tag{14}$$

$$H(x) = \{1 - wx[r_0 + \frac{1-2r_0x}{2}\ln\frac{1+x}{x}]\}^{-1} \tag{15}$$

$$B(g) = \frac{B_0}{1 + \frac{1}{h}\tan\frac{g}{2}} \tag{16}$$

$$r_\lambda(i,e,g) = \frac{w}{4\pi}\frac{\mu_0}{\mu+\mu_0}[(1+B(g))p(g) + H(\mu_0)H(\mu) - 1]sr^{-1} \tag{17}$$

$$REFF(i,e,g) = \frac{\pi}{\mu_0} r_\lambda(i,e,g) \tag{18}$$

$$RADF(i,e,g) = \pi r_\lambda(i,e,g) \tag{19}$$

where w is the single-scattering albedo, $p(g)$ is the single particle phase function, b and c are material dependent constants that indicate the degree of scattering direction, $B(g)$ is the backscatter function, $H(\mu)$ and $H(\mu_0)$ are Chandrasekar's functions; M_j, ρ_j and d_j are mass fraction, average density and average dimension of the particles of the jth mineral phase, respectively; B_0 is the intensity of the opposition effect and h is the angular amplitude of this effect.

b and c are set to 0, that is to say the scattering is assumed isotropic, since no preferential orientation should occur in the regolith or in the laboratory samples. In addition, no backscattering is considered, since it is known (Mustard and Pieters, 1989) that Opposition Effect is negligible for phase angles larger than 15°. Chosen RELAB spectra are obtained with 30° phase angle, and for the selection of NIRS spectra to be modelled, angles between 28° and 32° have been chosen (Table 6).

The goodness of fits is evaluated using the R^2 statistical test, where

Table 2
RELAB spectra used in this work. Reported grain sizes are an average on minimum and maximum values of the sieve.

Class	Meteorite	Grain size	RELAB reference
L4	Saratov	5.0	MB-CMP-028-A/CAMB28
L4	Saratov	27.5	MB-CMP-028-B/CBMB28
L4	Saratov	69.5	MB-CMP-028-C/CCMB28
L4	Saratov	147.0	MB-CMP-028-D/CDMB28
L4	Saratov	285.0	MB-CMP-028-E/CEMB28
L5	Tsarev Light	12.5	RS-CMP-060-P6/P6RS60
L5	Tsarev Light	35.0	RS-CMP-060-P7/P7RS60
L5	Tsarev Light	54.0	RS-CMP-060-P8/P8RS60
L5	Tsarev Light	94.0	RS-CMP-060-P3/P3RS60
L5	Tsarev Light	187.5	RS-CMP-060-P4/P4RS60
L5	Tsarev Dark	10.0	RS-CMP-047-P8/P8RS47
L5	Tsarev Dark	32.5	RS-CMP-047-P9/P9RS47
L5	Tsarev Dark	54.0	RS-CMP-047-P10/P0RS47
L5	Tsarev Dark	94.0	RS-CMP-047-P5/P5RS47
L5	Tsarev Dark	187.5	RS-CMP-047-P6/P6RS47
L5	Tsarev Dark	375.0	RS-CMP-047-P7/P7RS47
LL5	Alta'ameem	62.5	MB-TXH-083/C1MB83
LL5	Alta'ameem	312.5	MB-CMP-013/C1MB13
LL6	Yamato-74646	12.5	MB-TXH-085-C/CAMB85
LL6	Yamato-74646	35.0	MB-TXH-085-B/CBMB85
LL6	Yamato-74646	60.0	MB-TXH-085-C/CCMB85
E	ALHA76005	12.5	MB-TXH-066-A/CAMB66
E	ALHA76005	35.0	MB-TXH-066-B/CBMB66
E	ALHA76005	60.0	MB-TXH-066-C/CCMB66
E	ALHA76005	100.0	MB-TXH-066-D/CDMB66
E	ALHA76005	187.5	MB-TXH-066-E/CEMB66
E	ALHA76005	375.0	MB-TXH-066-F/CFMB66
E	Juvinas	12.5	MB-TXH-070-A/CAMB70
E	Juvinas	35.0	MB-TXH-070-B/CBMB70
E	Juvinas	60.0	MB-TXH-070-C/CCMB70
E	Juvinas	100.0	MB-TXH-070-D/CDMB70
E	Juvinas	187.5	MB-TXH-070-E/CEMB70
E	Millbillbillie	12.5	MB-TXH-069-A/CAMB69
E	Millbillbillie	35.0	MB-TXH-069-B/CBMB69
E	Millbillbillie	60.0	MB-TXH-069-C/CCMB69
E	Millbillbillie	100.0	MB-TXH-069-D/CDMB69
E	Yamato-74450	12.5	MB-TXH-071-A/CAMB71
E	Yamato-74450	35.0	MB-TXH-071-B/CBMB71
E	Yamato-74450	60.0	MB-TXH-071-C/CCMB71
E	Yamato-74450	187.5	MB-TXH-071-D/CCMB71
H	EET87503	12.5	MB-TXH-067-A/CAMB67
H	EET87503	35.0	MB-TXH-067-B/CAMB67
H	EET87503	60.0	MB-TXH-067-C/CAMB67
H	EET87503	100.0	MB-TXH-067-D/CAMB67
H	EET87503	187.5	MB-TXH-067-E/CAMB67
L4	Saratov	Slab	MR-MJG-046/CGN071
L5	Farmington	Slab	MR-MJG-077/CGN155
L6	Kunashak	Slab	RS-CMP-062/C1RS62
LL3	Krymka	Slab	RS-CMP-063/C1RS63
LL5	Chelyabinsk (L)	Slab	MT-PMJ-216/BKR1MT216
LL5	Olivenza	Slab	MR-MJG-071/CGN139
LL5	Alta'ameem	Slab	OC-TXH-010-A/C1OC10A
LL6	Cherokee Springs	Slab	OC-TXH-001-A/C1OC01A

Table 3
Reference mineral abundance values for Itokawa (Tsuchiyama et al., 2014), for Alta'ameem (Dunn et al., 2010), and for the pyroxene mixtures (Sunshine and Pieters, 1993).

Object	Grain size (μm)	Olivine %	HCP %	LCP %	PL %	Opaque %
Itokawa	unknown	67.17	2.58	18.1	8.5	3.65
Alta'ameem	0–125	51.1	7.9	23.3	9.0	8.7
Mixture 1	0–45, 45–75, 75–125	0	85	15	0	0
Mixture 2	0–45, 45–75, 75–125	0	50	50	0	0
Mixture 3	0–45, 45–75, 75–125	0	15	85	0	0

Table 4
Endmembers considered for Hapkes modelling. Refraction index (n) and density (ρ) were computed as a weighted average between their component minerals. We considered values of density and index of refraction from Deer et al. (2013).

Samples grain size 0 – 45 μm		
	n	$\rho(g/cm^3)$
HCP		
Augite	1.70	3.40
Wo 15% En 34% Fs 51%	1.70	3.53
Wo 20% En 64% Fs 16%	1.67	3.25
Wo 20% En 30% Fs 45%	1.69	3.45
Wo 30% En 49% Fs 21%	1.67	3.25
Wo 35% En 0% Fs 65%	1.71	3.56
Wo 40% En 48% Fs 12%	1.66	3.15
Wo 50% En 40% Fs 10%	1.66	3.10
Wollastonite	1.64	2.84
Diopside	1.69	3.40
LCP		
Fs_{20}	1.68	3.35
Fs_{25}	1.68	3.39
Fs_{30}	1.69	3.43
Fs_{65}	1.72	3.69
Hypersthene	1.72	3.55
OL		
Fo_{40}	1.76	3.94
Fo_{50}	1.75	3.83
Fo_{60}	1.74	3.72
Fo_{70}	1.73	3.61
Fo_{80}	1.72	3.49
Fo_{90}	1.71	3.38
PL		
$An_{0.1}$	1.54	2.63
$An_{1.6}$	1.61	2.80
$An_{9.8}$	1.98	3.70
$An_{14.4}$	2.19	4.20
$An_{23.5}$	2.60	5.21
$An_{52.8}$	3.92	8.43
Labradorite	1.56	2.69

Table 5
HCP and LCP endmembers used for Test 1. Refraction index and density have been calculated as a weight average between the minerals that compose every endmember.

	Wo%	En%	Fs%	n	$\rho(g/cm^3)$
HCP	46	46	9	1.68	3.13
LCP	1	87	12	1.67	3.29

Table 6
Geometric information associated to the NIRS selected spectra, corresponding to the five regions labelled in Fig. 4.

Label	Centre latitude(°)	Centre longitude(°)	Phase angle(°)	Incidence angle(°)	Emission angle(°)	Terrain
A	−0.83	3.34	29.32	63.39	40.38	rough
B	−16.95	46.10	30.86	70.15	46.21	smooth
C	0.61	110.71	31.48	71.85	42.81	rough
D	18.51	171.97	28.21	70.81	57.54	rough
E	39.96	256.40	33.65	49.43	68.55	smooth

R^2 is defined as:

$$R^2 = 1 - \frac{\sum_i (Y_{obs} - Y_{fit})^2}{\sum_i (Y_{obs} - \bar{Y}_{obs})^2} \quad (20)$$

where Y_{obs} and Y_{fit} are the real and modelled spectra, respectively. If $R^2 = 1$, then the model perfectly describes the real function.

3.2.4. Endmembers

The simplest approach to apply the Hapke's modelling to synthetize

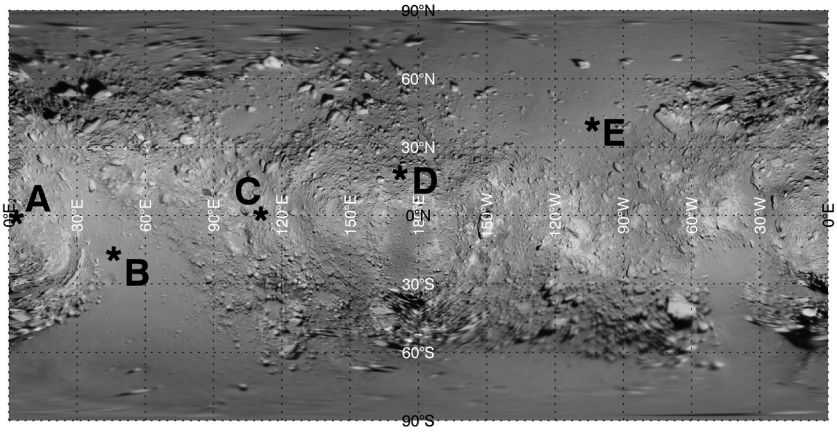

Fig. 4. Selected regions of Itokawa. The map is a cylindrical projection from P. (2012). B and E spectra are taken from smooth terrains, respectively placed in the regions named Muses Sea (where Hayabusa took its samples) and Sagamihara. A and D spectra are placed on the head and on the bottom of the body, respectively. C is a random rich-in-boulders place on the body.

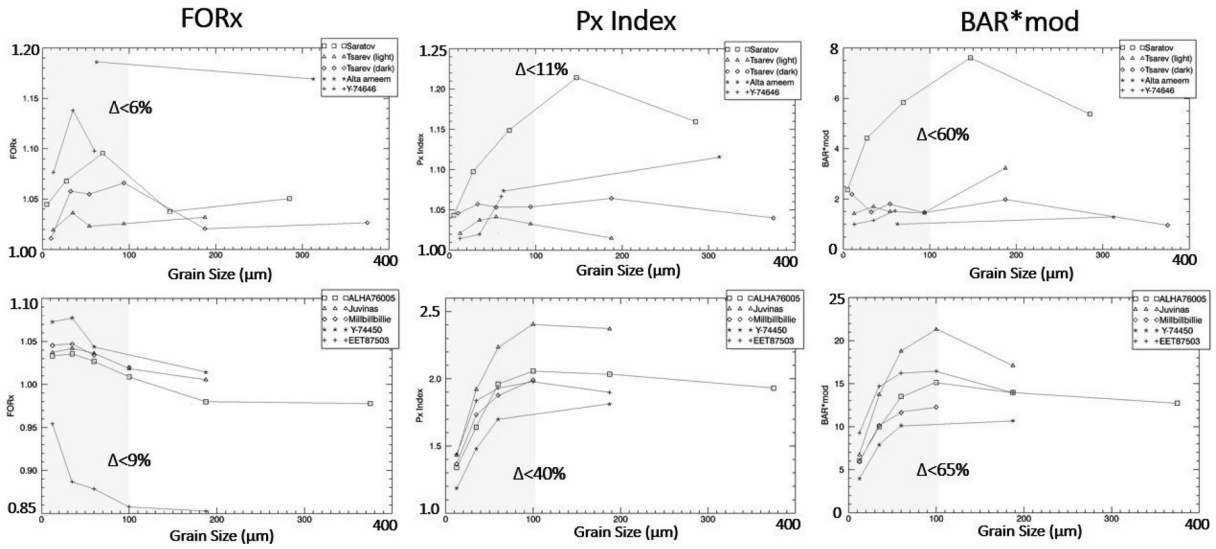

Fig. 5. FORx (left), Modified BAR* (centre), and Px Index (right) calculated for different grain sizes on ordinary chondrites (top) and HED samples (bottom).

Table 7
Olivine abundances from previous works (indicated in the legend). The Olivine % column is the absolute abundance of olivine in the meteorite, whilst Normalized Olivine % is the olivine/(olivine + pyroxene) value. Very different values for the olivine content in a single meteorite can be related to differences in the analysed samples or to different experimental technique used. No uncertainities are reported since they are not present in most of the references.

Class	Meteorite	Reference	Olivine %	Normalized Olivine %	References	
L4	*Saratov*	MS	38.88	53.12	Oshtrakh et al. (2008)	OS
		OS	51.64	70.35	Albassam (1978)	AL
L5	*Farmington*	OS	43.44	64.14	Dunn et al. (2010)	DU
L6	*Kunashak*	MS	46.95	62.97	McSween et al. (1991)	MS
		OS	59.84	75.75	Galimov et al. (2013)	GA
		Du	43.90	59.81		
LL3	*Krymka*	MS	53.61	66.15		
LL5	*Chelyabinsk (L)*	GA	60.7	77.52		
LL5	*Olivenza*	MS	53.29	66.74		
		DU	51.00	63.99		
LL5	*Alta'ameem*	AL	53.00	70.29		
		DU	51.10	62.09		
LL6	*Cherokee Springs*	MS	54.08	68.10		
		DU	51.20	66.58		

a spectrum would be to mix a large number of endmembers in order to find the best fitting composition. Since this approach is very expensive from a computational point of view, an initial guess of the composition in order to put some initial constraints to the analysis is needed. In this work, the values in Table 3 have been taken as reference values and the endmembers in Table 4 have been used to fit Itokawa's spectra. The same endmembers have been used to fit an Alta'ameem meteorite spectrum used in the testing phase along with pyroxene mixtures in Table 5. Test phase will be discussed in Section 4. In Table 3 "opaque" column refers to all the minerals that are not olivine, pyroxene or plagioclase. This approximation is quite reasonable, since in the case of the samples we are considering minor components are mainly composed by troilite (up to 70%; Tsuchiyama et al., 2014), which is one of the most widespread opaque mineral in S asteroids. The opaque spectra

Table 8
Range of olivine abundance (%) inferred by extrapolation from Table 1, assuming that selected chondrites are binary, HCP ternary, or LCP ternary mixtures. Binaries (Bin), HCPs, and LCPs columns are given in olivine abundance (%). Fx, Px and BA columns respectively indicate Forsterite Index, Px Index, and Modified BAR*. The errors are likely to be on the order of 10^{-2} for FORx and Px Index and on the order of 10^{-1} for Modified BAR*, as in Table 1, but it was impossible to explicitly calculate them since most of RELAB spectra comes without their standard deviation.

Meteorite	Fx	Bin	HCP	LCP	Px	Bin	HCP	LCP	BA	Bin	HCP	LCP
L4 Sarat.	1.06	50–70	30–40	55–65	1.03	70–90	70–80	75–85	1.8	70–90	60–70	70–80
L5 Farm.	1.01	50–60	0–20	40–50	1.06	70–90	70–80	70–80	3.8	70–90	40–50	60–70
L6 Kun.	1.02	50–60	0–20	45–55	1.13	70–90	60–70	65–75	4.4	70–90	30–40	60–70
LL3 Krym.	0.99	45–55	0–20	35–45	1.12	70–90	60–70	70–80	3.0	70–90	50–60	70–80
LL5 Chel.	1.02	50–70	15–25	45–55	1.15	70–90	50–60	65–75	3.2	70–90	50–60	70–80
LL5 Oliv.	1.15	70–90	65–75	75–85	1.11	70–90	70–80	70–80	1.0	70–90	70–80	80–100
LL5 Alta'am.	1.16	70–90	70–80	75–85	1.06	70–90	70–80	70–80	0.7	70–90	75–85	80–100
LL6 Cherok.	1.10	70–80	50–60	65–75	1.21	70–80	40–50	60–70	3.4	70–90	40–50	70–80

Table 9
Average values (on Home Position data) of spectral indices and inferred olivine abundances for Itokawa. The errors are given as standard deviation.

Index	Value	Δ	Binary	HCP	LCP
FORx	1.15	± 0.01	70–90	65–75	75–85
Px Index	0.97	± 0.01	90–95	80–90	80–90
BAR*mod	0.97	± 0.02	70–90	70–80	80–100

are defined as a null single scattering albedo spectrum with the density of troilite (4.61 g/cm^3).

3.2.5. Selection of NIRS spectra

Five Home Position spectra have been selected from five potentially different regions, labelled in Fig. 4. B and E spectra are taken from smooth terrains, respectively placed in the regions named Muses Sea (where Hayabusa took its samples) and Sagamihara. A and D spectra are placed on the head and on the bottom of the body, respectively. C is a random rich-in-boulders place on the body. In Table 6, information about the selected spectra is reported. The selection of spectra has been based on phase angle, too. Phase angles were taken around 30° to remove any possible issue due to opposition effect and to differences in observational geometry between RELAB and NIRS spectra.

4. Results

4.1. Calibration of spectral indices results

4.1.1. Grain size dependence

To show the dependence of spectral indices with grain size, spectra from meteorite sampled at different grain size have been analysed.

Fig. 5 shows FORx, Px Index, and Modified BAR* as a function of grain size for Saratov, Tsarev (light and dark fragments), Alta'ameem, and Y-74646 chondrites (top), and for some HED meteorites (bottom).

The general trend for ordinary chondrites is a larger variation of all the indices for smaller grain sizes, and a weak variation for greater grain sizes; FORx is the less affected by grain size among the three indices, as indicated by the lowest relative variability for grain sizes up to 100 m. This agrees with the results obtained by Palomba et al. (2015).

4.1.2. Dependence on olivine content

From binary, HCP ternary, and LCP ternary mixtures (Table 1), we obtained relations between olivine abundance and spectral indices (Fig. 3). Then we used these relations to infer olivine abundance from meteorite samples with known mineralogy. Itokawa is known to be analogue to LL chondrites (Tsuchiyama et al., 2014), but the relations have also been applied on some L chondrites in order to test them with a different meteorite class.

The results in olivine abundance (%) have to be interpreted as Ol/(Ol + Px) ratios (reported hereafter as "Normalized Olivine %"), and not as the absolute olivine content.

However, it is possible to notice that by empirically comparing the normalized and modal values reported in Table 7, two relations can be found for L and LL chondrites, respectively.

$$Modal\ Olivine\ in\ L\ chondrites\% = Normalized\ Olivine\% - 20\% \pm 6\% \quad (21)$$

$$Modal\ Olivine\ in\ LL\ chondrites\% = Normalized\ Olivine\% - 15\% \pm 5\% \quad (22)$$

Eq. (22) will be used to infer modal olivine abundance on Itokawa.

The results of these analyses are not clear for L chondrites, since different laboratory reference values for the same chondrite (Table 7) fit different olivine intervals inferred in Table 8. This fact may be due to both differences in samples and retrieval techniques used by the authors of those works. A meteorite may indeed show a heterogeneous composition, which results in different mineral content of different samples.

Nevertheless, for LL chondrites, olivine abundances found in literature and reported in Table 6 are more consistent one with each other. FORx is not able to predict olivine abundance for Krymka and Chelyabinsk, but this is expected since the threshold for FORx olivine detection found by Poulet et al. (2007) is 1.04 (and Krymka and Chelyabinsk have 0.99 and 1.02). This is not threatening, since Itokawa's values range between 1.09 and 1.20. For the other three LL chondrites, however, almost all the indices seem to predict the correct olivine ratios, at least within a 10%. This mean that no index may be excluded through this analysis, and that the three indices may be capable of retrieving olivine abundance at least for LL chondrites when FORx is higher than 1.02.

4.2. Indices on Itokawa

The average values of the three indices on Itokawa are reported in Table 9 together with inferred normalized olivine abundances.

The Modified BAR* has a systematic dependence with the distance from the asteroid surface (Fig. 6). The interpretation of such effect is not clear, but it is the result of a reflectance increase at the latest NIRS wavelengths, which causes a decrease in Band IIb in Eq. (3).

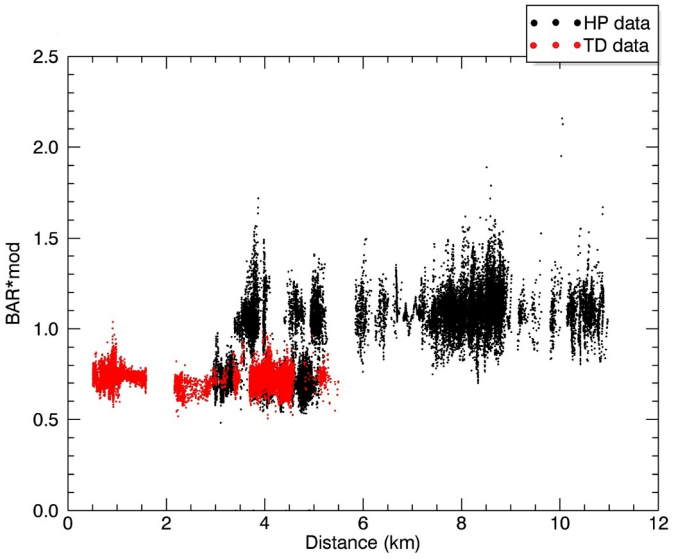

Fig. 6. Modified BAR* versus distance in HP (black) and TD (red) phases. (For interpretation of the references to colour in this figure legend, the reader is referred to the web version of this article.)

In Fig. 7, olivine/(olivine + pyroxene) ratio obtained using FORx is mapped on Itokawa's surface. Modified BAR* and Px Index have not been used due to their wide dependence on grain size (and distance in the case of Modified BAR*). The dots correspond to central latitude and longitude of the pixels. (A), (B), and (C) panels report the abundances inferred using Binary, LCP, and HCP mixtures from Table 1. In every panel, the top map reports HP data, while the bottom one reports TD ones. The reported abundances are the central values of the inferred intervals, so every value has to be intended with an uncertainty of ± 5%. If the olivine abundance is inferred from binary, HCP, and LCP mixtures, almost every point on the map result to be about 80%, 70%, and 85%, respectively. These values are consistent within a 10% with the expected values for Muses Sea in Table 3. However, variability is found on the Sagamihara region (North-East region in Fig. 7), which shows an olivine content up to 10% lower. This variability is not recognisable by using binary mixtures, because of their wider olivine abundance resolution. A little olivine increase is also observed in Fig. 7B (bottom), and in Fig. 7C (top) at the bottom of the body (centre of the map), where it is up to 10% higher, but it is present only in some maps, and hence it should be confirmed.

In Table 10, the average olivine abundance, which corresponds to FORx = 1.15, is reported. Following Table 1, this FORx value corresponds to 70–90% normalized olivine abundance for binary compounds, 65–75% normalized olivine abundance for HCP ternary compounds and 75–85% normalized olivine abundance for LCP ternary compounds. Tsuchiyama et al. (2014) reported a value for normalized olivine abundance on Itokawa of 76.46%. This value is inside the interval given by binary and LCP mixtures and it is only a 1.46% away from the HCP interval. By using Eq. (22) to remove the normalization, the olivine abundance from Tsuchiyama et al. (2014) becomes 67.17%, which is inside binaries and LCPs intervals (50-80% and 55–75%, respectively), and it is 2.17% from the HCPs interval (45–65%). Reported ntervals has to be assumed as 1-sigma intervals.

4.3. Synthetic spectra

4.3.1. Method validation

Two tests were performed in order to define the reliability of the described method. The first one is made using fully controlled pyroxene mixtures, while the second one was performed on a Alta'ameem meteorite sample, where grain size interval was wider (0–125 μm) and composition may be less precise due to a higher level of heterogeneity.

Test 1: Pyroxene mixtures. The pyroxene mixtures here used for testing are the ones analysed by Sunshine and Pieters (1993). They consist of nine spectra from HCP and LCP mixtures with known compositions, mass fractions, and grain sizes. In Table 5 the composition of the HCP and LCP endmembers is reported together with their index of refraction and density, computed as in Table 4.

Every mixture was available in three grain sizes intervals: 0–45 μm (Mixture 1), 45–75 μm (Mixture 2), and 75–125 μm (Mixture 3). Samples used as endmembers (Table 5) to reproduce these mixtures were available at 0–25 μm and at 45–75 μm grain sizes.

The results of these test are reported in Table 11 and in Fig. 8. The error range of 5% for mass fractions, and of 1 μm for grain sizes are due to the resolution chosen for HCP and LCP content variation.

Starting with endmembers seized at 45–75 μm it is possible to fit much better the expected values than starting with 0–25 μm, especially when trying to fit the highest grain size mixtures. This is an expected result, since the sizes in the smaller interval (0–25 μm) are nearly commensurate with the wavelengths (0.8-2.1 μm), making the basic assumptions made for the Hapke's equations not entirely applicable. In addition, evaluating as effective grain size the mean size of the sieve (12.5 μm) to calculate the optical constants at the beginning of the procedure may be not a good assumption for this grain size range since in dusty samples grain distribution may be different from a gaussian peaked at the mean size of the sieve. On the other hand, for the distribution 45–75 μm the optical constants calculated with a grain size of 60 μm should in principle approximate quite well the effective size of the distribution, since no fine powder are involved. Indeed, the fit is very good and R^2 is more than 0.99 for the 45–75 μm and 75–125 μm mixtures fitting. The fit is still good but with a lower R^2 for the 0–45 μm mixtures. Nevertheless, the resulting compositions match the expected ones within a 5% for these, too.

Test 2: Alta'ameem. A second test was needed in order to understand if the 0–45 μm grain size range, which is the one in which most of the needed minerals are present on the RELAB database, shows the same commensurativity-issue of the 0–25 μm range with wavelength range reported in Test 1. In order to perform this test with the same endmembers used for Itokawa, the meteorite of Alta'ameem has been chosen because of its mineralogical proximity to it. The test was positive, demonstrating that 0–45 μm endmembers did not have the same size-wavelength issue found with 0–25 μm endmembers.

In Table 3 the abundance of the mineral phases found in the meteorite is reported (Olivine: 51.1%; HCP: 7.9%; LCP: 23.3%; Plagioclase: 9.0%; opaques: 8.7%), but the grain size distribution is wider (0–125 μm) the pyroxene mixtures, and the composition and iron content of every mineral phase is unknown. The endmembers in Table 4 have been used to perform this test.

Referring to the mineralogical composition of the Alta'ameem meteorite in Table 3, the following constraints have been imposed:

- Opaque mass fraction was fixed to 8.7%;
- Olivine mass fraction has been varied between 41% and 61% with a resolution of 5%;
- Plagioclase mass fraction has been varied between 7% and 13% with a resolution of 2%;
- Pyroxene was set as complementary to the other mineral phases;
- HCP/LCP ratio could be 0.25, 0.5, or 0.75;
- Grain size varied between 25 and 125 μm with a 10 μm resolution.

The results reported in Table 12 and in Fig. 9 (top left) have been found. The best fit had a typical value of 0.97 for R^2. The found effective grain size is near the mean of the sieve, being 65 ± 10.

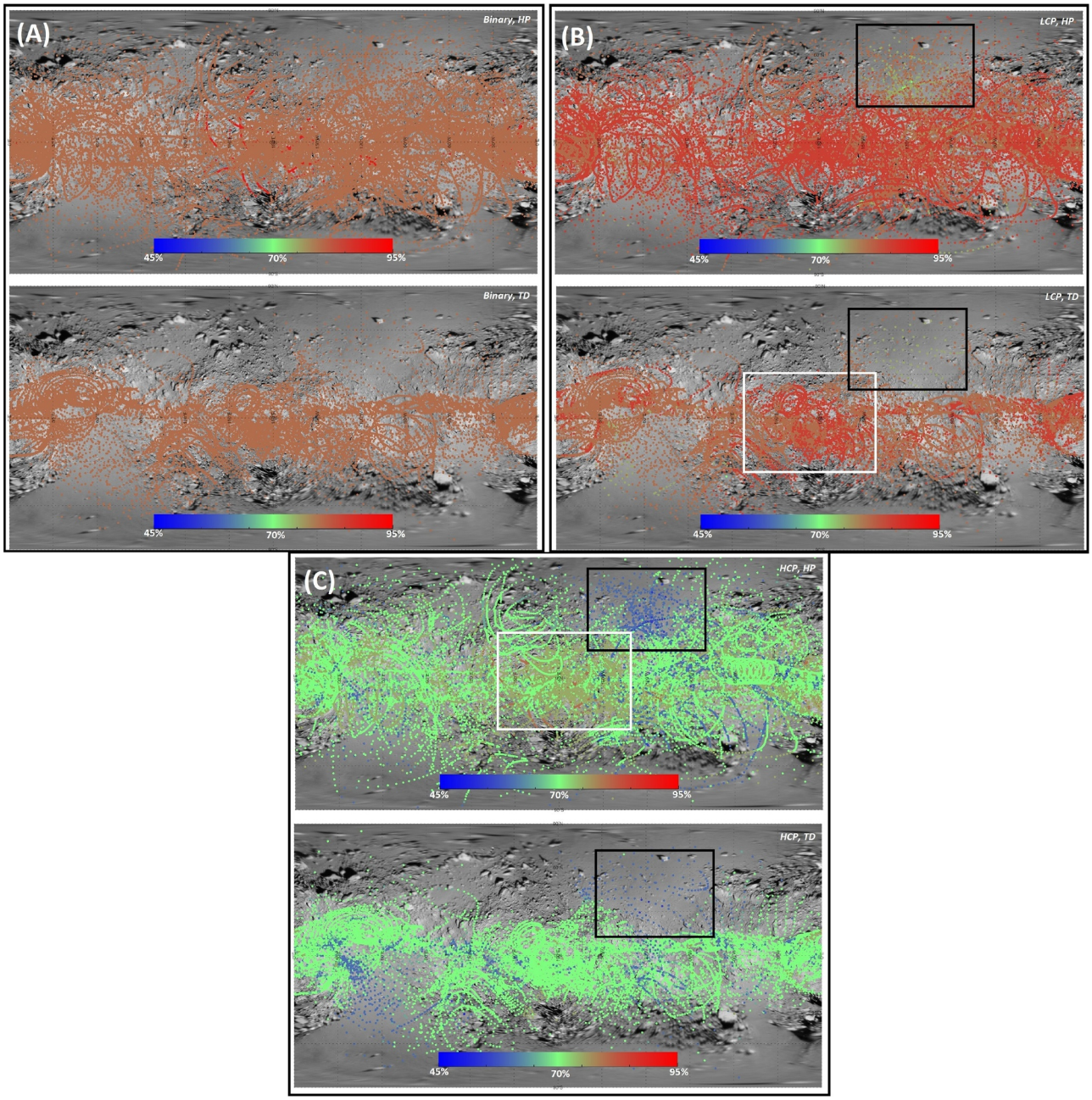

Fig. 7. Olivine/(olivine + pyroxene) mapping on Itokawa's surface using FORx. (A), (B), and (C) report the abundances inferred using Binary, LCP, and HCP mixtures from Table 1. In every panel, the top map reports HP data, while the bottom one reports TD ones. Black squares highlight the Sagamihara olivine reduction regions, while white squares highlight the increase at the bottom of the body.

Table 10
Normalized and non-normalized olivine content for FORx = 1.15. Expected column contains the values from Tsuchiyama et al. (2014), the others are the ones inferred from Table 1 and calculated through Eq. (22).

FORx = 1.15				
	Reference	Binary	HCP	LCP
Normalized Olivine %	76.46	70–90	65–75	75–85
Olivine %	67.17	50–80	45–65	55–75

4.4. Itokawa

Creating a synthetic spectrum that is able to fit a NIRS spectrum is much more complicated than fitting spectra from laboratory samples. RELAB samples usually do not present differences in grain size between mineral phases, whilst on a real case it is possible to find different grain sizes for different minerals, depending for example on their resistance to space weathering and comminution. In addition, the grain size in laboratory samples is given by the sieve, whilst we do not have strong constraints on Itokawa's grain size. Indeed, AMICA images revealed particles down to 1 mm size (Yano et al., 2006), but it is not possible to exclude the presence of smaller particles so far. Actually, smaller particles are very likely to be present on the asteroid surface, and they would have a strong impact on the resulting spectrum.

4.4.1. Darkening effects

The best combination of endmembers leads to model spectra that are steeper and brighter than the NIRS one. The difference cannot be ascribed to observation geometry, taken into account by the Hapke modelling. By choosing a null spectrum for opaque component, as in

Table 11
Results for pyroxenes mixture test. Every abundance has a 5% uncertainty and every grain size has a 1 μm uncertainty.

Sample	HCP/LCP	Sample grain size (μm)	HCP/LCP best fit (± 5/5)	Grain size best fit (± 1 μm)	R^2
Endmembers	0–25 (μm)				
Mixture 1	85/15	0–45	75/25	13	0.99
Mixture 1	85/15	45–75	85/15	47	0.98
Mixture 1	85/15	75–125	85/15	83	0.99
Mixture 2	50/50	0–45	35/65	13	0.98
Mixture 2	50/50	45–75	35/65	50	0.94
Mixture 2	50/50	75–125	35/65	82	0.91
Mixture 3	15/85	0–45	0/100	14	0.93
Mixture 3	15/85	45–75	0/100	51	0.86
Mixture 3	15/85	75–125	0/100	89	0.86
Endmembers	45–75 (μm)				
Mixture 1	85/15	0–45	80/20	17	0.98
Mixture 1	85/15	45–75	85/15	67	0.99
Mixture 1	85/15	75–125	85/15	119	0.99
Mixture 2	50/50	0–45	50/50	15	0.95
Mixture 2	50/50	45–75	55/45	57	0.99
Mixture 2	50/50	75–125	55/45	96	0.99
Mixture 3	15/85	0–45	20/80	15	0.97
Mixture 3	15/85	45–75	15/85	51	0.99
Mixture 3	15/85	75–125	15/85	98	0.99

this work, it should be reasonable that the resulting fits were darker than the real ones instead of being brighter. Therefore, it was necessary to find another darkening source in order to explain the reflectance values of NIRS spectra.

It has been found that decreasing the grain size of the opaque component may bring to the desired darkening effect. In particular, it has empirically been found that a grain size of about 3 μm for this component produces good fits. This constraint would mean that if the boulders and the regolith of Itokawa are covered with dark dust particles, they would undergo a strong spectral darkening effect. These particles would not be seen on AMICA's images due to resolution constraints, but they are likely to exist.

4.4.2. Constraints

On the basis of previous works (Tsuchiyama et al., 2014), and on the results obtained through spectral indices, the following constraints on mass fractions have been imposed.

- Olivine mass fraction may varies between 45% and 70%, with a resolution of 5%.
- Plagioclase mass fraction was fixed to 8.5%, that is the value from Tsuchiyama et al. (2014). It has been verified with some tests that introducing a variability in this value did not improve significantly the fitting procedure, whilst it strongly increased computational time.
- Pyroxene mass fraction was complementary to the others, and divided into 25% HCP and 75% LCP. Anyway HCP/LCP ratio was not fixed in this way, since the HCP endmembers in Table 4 are mixtures of Wo (HCP), Ferrosilite and Enstatite (LCPs) with variable relative abundances.
- Grain sizes for bright components were between 10 and 100 μm, with a resolution of 10 μm. Grain size for the dark components may vary between 3.0 and 3.8 μm, with a resolution of 2 μm.

By applying these constraints, about 6×10^5 spectra were created.

4.4.3. Results

The obtained mineralogy of the five selected Itokawa's spectra are shown in Tables 13 and 14. All the fits have a R^2 included between 0.98 and 0.99. Table 13 reports the whole interval of values found for fits with R^2 greater than 0.98, whilst Table 14 reports only the best fitting

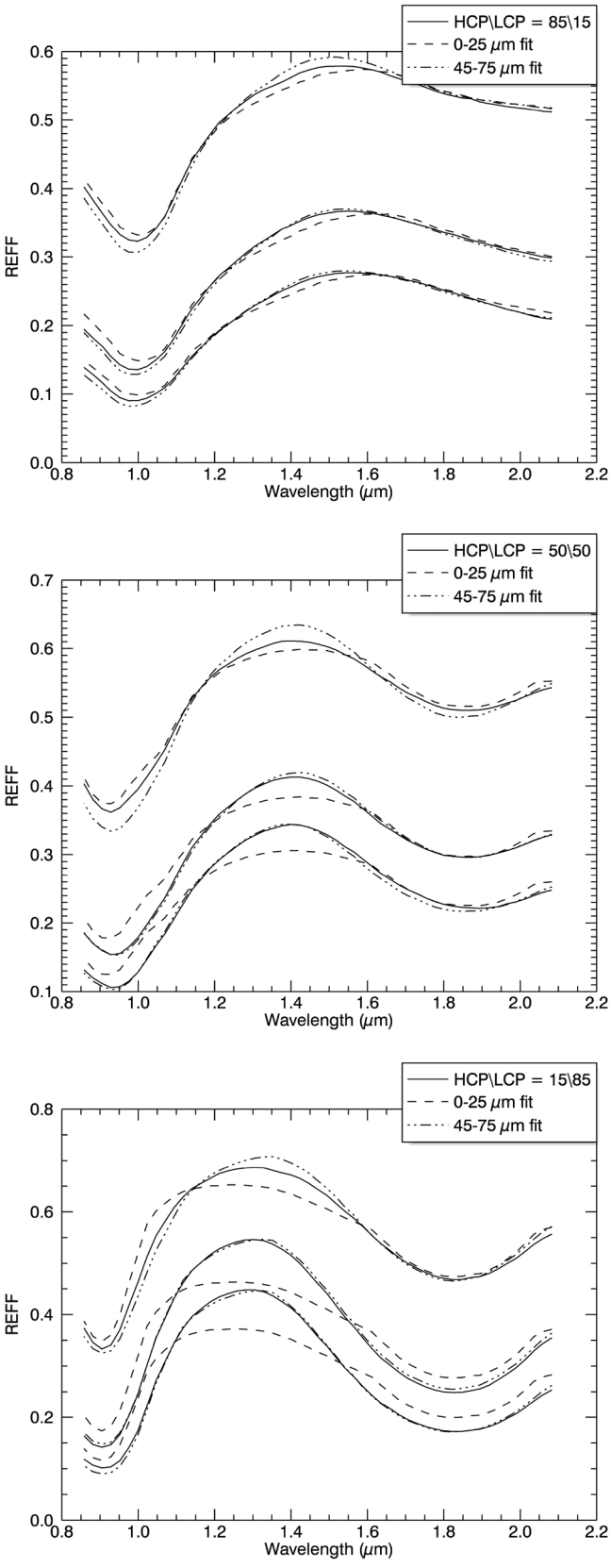

Fig. 8. HCP/LCP = 85/15 (top), 50/50 (middle), 15/85 (bottom) mixture fitting. In every plot, from top to bottom: 0–45 μm, 45–75 μm, and 75–125 μm grain size mixtures. Dashed lines and dot-dashed lines refer to model spectra synthetized using respectively endmembers with 0–25 μm or 45–75 μm.

Table 12
Results from Alta'ameem spectrum fitting. Reference values are from Dunn et al. (2010).

	Olivine%	HCP%	LCP%	PL	Opaque %	Grain size (μm)
Reference	51.1	7.9	23.3	9.0	8.7	0–125
Modelled	51 ± 5	3 ± 1	27 ± 7	11 ± 2	8.7	65 ± 10
Type	Fo_{90}	Wo	Fs_{52}	$An_{52.8}$	~troilite	

abundances (R^2 values reported in Fig. 9 legends). The intervals include the error bars due to the chosen resolution (± 5 for olivine, ± 1 for HCP, ± 4 for LCP, ± 10 μm for the grain size of bright components and ± 0.2 μm for that of the dark component). The grain size for the dark component in Table 13 is always 3.4 ± 0.4 μm, whilst in Table 14 they are specified in the Grain Size column.

4.5. Comparison between the two methods

In Table 15, a comparison with the olivine abundance derived with the two methods is reported. The reported values are consistent with each other. The FORx method has a larger uncertainty because it has a wider resolution (10%) and the Eq. (22) used to retrieve olivine abundance from olivine/(olivine + pyroxene) widen more the error range, increasing it by another ± 5%. The second method is more accurate (uncertainties within a 5%), but it needs a great number of inputs and assumptions that may significantly influence the retrieved values.

5. Discussion

Fig. 7 shows that the surface of Itokawa appears to be quite homogeneous in olivine content, even if a few variability is present. However, variability is found on the Sagamihara region, which shows an olivine content up to 10% lower.

The lower olivine content retrieved on Sagamihara cannot be ascribed to a different grain size, since the same reduction is not seen in Muses Sea (South-West region in Fig. 7), on which terrain is equally smooth. Smooth regions are poor in boulders and rich in fine-grained regolith. Then, if grain size influenced olivine abundance, the retrieval in both these regions would have undergone the same influence and then a similar reduction in olivine. This fact may lead to conclude that grain size distribution on Itokawa is not olivine-dependent. Indeed, if there was a relation between olivine content and grain size, Muses Sea and Sagamihara would have had a similar olivine content. This could be possible because similar degree of space weathering and comminution may influence grain size parameter depending on grains composition. Since this is not found, we can exclude this kind of relation on Itokawa.

In principle, different values of spectral indices may be related to space weathering effects, too. It is expected that space weathering sources act homogeneously on the whole surface. Again, if different degree of space weathering are related to different size of the grains, a similar effect should be found on Muses Sea (and this is not the case). In addition, the samples used to calibrate the indices are not weathered, and nevertheless the average results are in good agreement with the laboratory analysed particles (Tsuchiyama et al., 2014): this means that it is more likely that space weathering has only a slight influence on the retrieved abundances, not detectable with the methods used in this work.

Values for both olivine and pyroxene abundance inferred by modelling the B spectrum are in good agreement with values found in Muses Sea particles (Tsuchiyama et al., 2014), and this is very important to evaluate the goodness of the retrieval. Hayabusa was indeed a sample-return mission, and comparing laboratory analyses with remote spectroscopy results may give a strong validation of the method. Since the agreement is good, it can be assumed that the results found in the other regions are in good agreement with the real olivine abundance, too. Even if in this work we focused our efforts on olivine retrieval, it should be noted that HCP and LCP abundances agrees well with the values found for Itokawa grains, too.

Even if we have no reference value for grain size to compare, we obtained a first estimate of it (e.g. 40 ± 10 μm in the B spectrum). In addition, we found that the whole asteroid seems to be covered with a fine dusty darkening agent, with a size of about 3 μm.

The slight shortward shift of absorption bands in model spectra with respect to NIRS spectra could be due to the specific composition of the mineral phases and not to their abundances. In particular, this is strongly evident in the LCP iron content in Table 14, where in the Muses Sea it is suggested Fs_{20-30}, instead of the Fs_{58-71} here considered. Differences in iron content would indeed bring to differences in band centres both in Band I and in Band II. Probably, these differences originate from the resolution chosen for mass fractions, iron content of endmembers and grain size. Using a finer resolution would improve the method but it would consistently increase the needed computational resources.

6. Summary and conclusions

In this work, two methods have been applied to retrieve abundance and distribution of olivine on Itokawa from Hayabusa/NIRS data. The two methods were defined because the classical approach based on the computation of band centre and band depths of the pyroxene absorption bands cannot be applied on NIRS data, because of the limited spectral range of the instrument.

The first method consists of the application of spectral indices. These are combinations of reflectances at different wavelengths and band parameters that have been found to be empirically related to the presence of olivine. The choice of the indices is obviously affected by the restricted spectral range of NIRS, too. Indeed, two indices that fit this spectral range have been chosen from literature (Px Index and Forsterite Index), and a third index has been developed (Modified BAR*). Px Index and Modified BAR* may have a strong dependence on grain size., especially when grain size is smaller than 100 μm . In addition, Modified BAR* presents a not completely understood dependence on distance that imposes a too strong constraint to its reliability. Regardless of its cause, this dependence is the result of differences in reflectance values in the last wavelengths, and then it may be an issue that exists only with this particular dataset. Then, it cannot be excluded that Modified BAR* may be successfully applied in future works. Anyway, these reasons brought to exclude Px Index and Modified BAR* from the mapping phase, since they jeopardise the reliability of the retrieval.

Forsterite Index values present a dependence on small grain sizes, too, but it is much weaker and so the lack of strong constraints on particles size has a lesser influence on results. Testing Forsterite Index on some ordinary chondrite samples, the inferred values of olivine abundance results to be consistent within a 10% with the abundances found in literature if their FORx is greater than 1.04, which is the detection threshold found by Poulet et al. (2007).

Then, it has been chosen to map the abundances inferred with the Forsterite Index on the surface of Itokawa, since it proved to be sufficiently reliable. From this mapping, the surface of Itokawa appears to be quite homogeneous in olivine content, even if some variability is present, especially in the region of Sagamihara, where it results to be up to 10% lower than in the other regions. This reduction of olivine abundance may be due to a different formation history of this region, consistently with its rubble pile structure, that is to say that it is an agglomerate of debris that potentially may originate from mineralogically different sources.

From this analysis, the resulting olivine/(olivine + pyroxene) average value for Itokawa is 75 ± 10, which is consistent with the

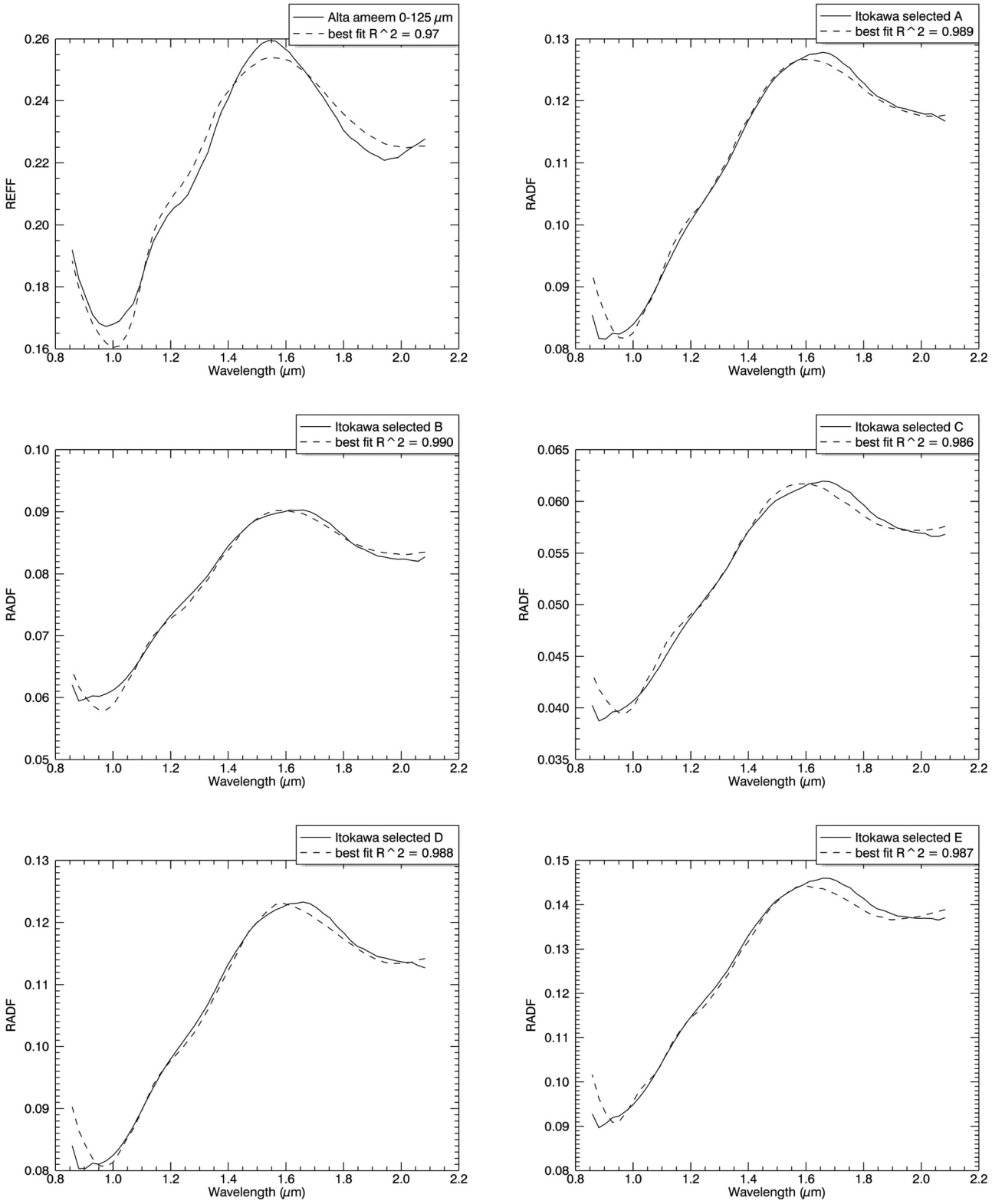

Fig. 9. Best fit for Alta'ameem spectrum (top left) and NIRS selected spectra.

value found in previous works (e.g. Binzel et al., 2001). Using an empirically found relation, this corresponds to an average absolute olivine abundance of 60 ± 15%. This value agrees with Tsuchiyama et al. (2014) in the particles of Muses Sea sampled by the probe. This result has important implication about the olivine distribution on Itokawa, since it means that Muses Sea particles are good representative of the whole Itokawa's surface, with the exception of Sagamihara region. Itokawas olivine average abundance classifies it as a potential source of ordinary chondrites.

Spectral indices results may be quickly obtained and provide a good first guess for applying the Hapke's model to a selection of spectra, aimed to a more accurate retrieval.

Table 13
Results for the five selected regions of Itokawa with R^2 greater than 0.98. Reference values are based on the laboratory analysis reported by Tsuchiyama et al. (2014).

Label	Olivine %	HCP %	LCP%	PL %	Opaque %	Grain size (μm)
Reference (Muses Sea)	67.17 Fo_{70-80}	2.58	18.1 Fs_{20-30}	8.5 An_{10-20}	3.65 ~troilite	Unknown
Modelled						
A	50–70 Fo_{40-60}	1–9 any	13–29 Fs_{30-70}	8.5 any	3.65 ~troilite	30 ± 10
B	50–70 Fo_{50-60}	1–10 any	13–32 Fs_{30-65}	8.5 any	3.65 ~troilite	40 ± 20
C	40–70 Fo_{60-70}	1–12 any	13–36 Fs_{25-65}	8.5 any	3.65 ~troilite	70 ± 20
D	45–70 Fo_{40-60}	1–10 any	13–32 Fs_{50-65}	8.5 any	3.65 ~troilite	30 ± 10
E	40–70 Fo_{50-70}	1–12 any	13–32 Fs_{25-70}	8.5 any	3.65 ~troilite	60 ± 20

Table 14
Best fit results for the five selected regions of Itokawa. Reference values are based on the laboratory analysis reported by Tsuchiyama et al. (2014).

Label	Olivine %	HCP %	LCP%	PL %	Opaque %	Grain size (μm)
Reference (Muses Sea)	67.17 Fo_{70-80}	2.58	18.1 Fs_{20-30}	8.5 An_{10-20}	3.65 ~troilite	Unknown
Modelled						
A	65 ± 5 Fo_{60}	2 ± 1 *Wo*	21 ± 5 Fs_{71}	8.5 $An_{52.8}$	3.65 ~troilite	30 ± 10 op = 3.2 ± 0.2
B	65 ± 5 Fo_{60}	1 ± 1 *Wo*	22 ± 5 Fs_{65}	8.5 $An_{23.5}$	3.65 ~troilite	40 ± 10 op = 3.4 ± 0.2
C	60 ± 5 Fo_{60}	7 ± 1 *Wo*	21 ± 5 Fs_{65}	8.5 $An_{1.6}$	3.65 ~troilite	60 ± 10 op = 3.0 ± 0.2
D	60 ± 5 Fo_{50}	4 ± 1 *Wo*	25 ± 5 Fs_{58}	8.5 $An_{1.6}$	3.65 ~troilite	30 ± 10 op = 3.2 ± 0.2
E	55 ± 5 Fo_{60}	3 ± 1 *Wo*	29 ± 5 Fs_{71}	8.5 $An_{14.4}$	3.65 ~troilite	60 ± 10 op = 3.4 ± 0.2

Table 15
Comparison between olivine abundance inferred from the FORx and that derived by creating synthetic spectra for the 5 selected regions of Itokawa.

Label	FORx	Olivine % FORx binary	Olivine % FORx HCP	Olivine % FORx LCP	Olivine % synthetic best fit
Reference	(Muses Sea)	67.17	67.17	67.17	67.17
A	1.17 ± 0.01	50–80	50–70	60–80	60–70
B	1.15 ± 0.01	50–80	45–65	55–75	60–70
C	1.16 ± 0.01	50–80	50–70	60–80	55–65
D	1.16 ± 0.01	50–80	50–70	60–80	55–65
E	1.17 ± 0.01	50–80	50–70	60–80	50–60

The second method consisted on optical constants retrieval from RELAB mineral spectra. These have then been used with the equations from Hapke (2012) in order to create synthetic spectra with the desired composition and grain size. Among these synthetic spectra, the one which best fits the spectrum under analysis is considered to have a composition which is similar to it.

Five spectra from morphologically different regions have been modelled. The olivine abundance of the spectrum from Muses Sea was in good agreement with the value from laboratory analysis of samples returned by Hayabusa, validating our method. From this comparison, we could estimate the accuracy on retrieved content of olivine, HCP, and LCP within 5%, 2%, and 4%, respectively.

Combining these two methods proved to be a powerful technique in order to retrieve olivine abundance. The first method is very fast and can be applied to the whole dataset, giving a first guess on olivine abundance on a surface. This guess can be subsequently used in order to analyse with more detail a selection of spectra using a radiative transfer model in order to create syntethic spectra.

The whole analysis brings to results that confirm that Itokawa belongs to S asteroid complex and hence is a potential source of ordinary chondrites, especially of the LL chondrites. This means that Itokawa's origin is likely to be located in the inner Main Asteroid Belt, where S asteroids are more common.

Acknowledgements

The authors acknowledge the thorough help of Cristian Carli and Mauro Ciarniello from INAF-IAPS (Rome), who provided an important contribution to the development of the methods, and Ted Roush from NASA (Ames Research Center), who provided its computational tools useful to retrieve optical constants from mineral spectra.

Supplementary material

Supplementary material associated with this article can be found, in the online version, at doi:10.1016/j.icarus.2018.10.035.

References

Abe, M., Tagaki, Y., Abe, S., Kitazato, K., Hiroi, T., Ueda, Y., Vilas, F., Clark, B.E., Fujiwara, A., 2004. Characteristics and current status of near infrared spectrometer for Hayabusa mission. Lunar and Planetary Science XXXV.

Abe, M., Takagi, Y., Abe, S., Kitazato, K., 2011. Instrument calibration of the Hayabusa near-infrared spectrometer. Hayabusa NIRS Calibrated Spectra V1.0. HAY-A-NIRS-3-NIRSCAL-V1.0. NASA Planetary Data System.

Abe, M., Takagi, Y., Kitazato, K., Abe, S., Hiroi, T., Vilas, F., Clark, B.E., Abell, P.A., Lederer, S.M., Jarvis, K.S., Nimura, T., Ueda, Y., Fujiwara, A., 2006. Near-infrared

spectral results of asteroid Itokawa from the Hayabusa spacecraft. Science 312, 1334–1338.
Abell, P.A., Vilas, F., Jarvis, K.S., Gaffey, M.J., Kelley, M.S., 2007. Mineralogical composition of (25143) Itokawa 1998 SF36 from visible and near-infrared reflectance spectroscopy: evidence for partial melting. Meteorit. Planet. Sci. 42, 2165–2177. Nr 12
Albassam, K.S., 1978. The mineralogy and chemistry of the Alta'ameem meteorite. Meteoritics 13 (2).
Bhatt, M., Reddy, V., Le Corre, L., Sanchez, J.A., Dunn, T., Izawa, M.R.M., Li, J., Becker, K.J., Weller, L., 2015. Spectral calibration for deriving surface mineralogy of asteroid (25143) Itokawa from Hayabusa near-infrared spectrometer (NIRS) data. Icarus 262, 124–130.
Binzel, R.P., Rivkin, A.S., Bus, S.J., Sunshine, J.M., Burbine, T.H., 2001. MUSES-c target asteroid (25143) 1998 SF36: a reddened ordinary chondrite. Meteorit. Planet. Sci. 36, 1167–1172.
Burbine, T.H., 2017. Asteroids: Astronomical and Geological Bodies. Cambridge Planetary Science, pp. 367.
Carli, C., Roush, T.L., Pedrazzi, G., Capaccioni, F., 2016. Visible and near-infrared (VNIR) reflectance spectroscopy of glassy igneous material: spectral variation, retrieving optical constants and particle sizes by Hapke model. Icarus 266, 267–278.
Ciarniello, M., Capaccioni, F., Filacchione, G., Raponi, A., Tosi, F., De Sanctis, M.C., Capria, M.T., Erard, S., Bockelee-Morvan, D., Leyrat, C., Arnold, G., Barucci, A., Beck, P., Bellucci, G., Fornasier, S., Longobardo, A., Mottola, S., Palomba, E., Quirico, E., Schmitt, B., 2015. Photometric properties of comet 67p/churyumov-gerasimenko from VIRTIS-m onboard rosetta. Astron. Astrophys. 583, A31.
Clark, R.N., 1999. Spectroscopy of rocks and minerals, and principles of spectroscopy. In: Rencz, A.N. (Ed.), Manual of Remote Sensing for the Earth sciences: Manual of remote sensing, third ed. vol. 3. John Wiley and Sons Inc., New York, pp. 3–52.
Cloutis, E.A., Gaffey, M.J., Jackowski, T.L., Reed, K.L., 1986. Distribution for olivine-orthopyroxene mixtures from reflectance spectra. J. Geophys. Res. 91 (B11), 11641–11653.
Deer, W., Howie, R.A., Zussman, J., 2013. An introduction to the rock-forming minerals. Mineral. Soc. 498.
Dunn, T.L., Cressey, G., McSween Jr, H.Y., McCoy, T.J., 2010. Analysis of ordinary chondrites using powder x-ray diffraction: 1. modal mineral abundances. Meteorit. Planet. Sci. 45, 123–134. Nr 1, (2010)
Fujiwara, A., Kawaguchi, J., Yeomans, D.K., Abe, M., Mukai, T., Saito, J., Yano, H., Yoshiwaka, M., Scheeres, D.J., Barnouin-Jha, O., Cheng, A.F., Demura, H., Gaskell, R.W., Hirata, N., Ikeda, H., Kominato, T., Miyamoto, H., Nakamura, A.M., Nakamura, R., Sasaki, S., Uesugi, K., 2006. The rubble-pile asteroid Itokawa as observed by Hayabusa. Science 312, 1330–1334.
Galimov, E.M., Kolotov, V.P., Nazarov, M.A., Kostitsyn, Y.A., Kubrakova, I.V., Kononkova, N.N., Roshchina, I.A., Alexeev, V.A., Kashkarov, L.L., Badyukov, D.D., Sevast'yanov, V.S., 2013. Analytical results for the material of the Chelyabinsk meteorite. Geochem. Int. 51 (7), 522–539.
Hapke, B., 1981. Bidirectional reflectance spectroscopy: 1. Theory. J. Geophys. Res. 86 (B4), 3039–3054.
Hapke, B., 2012. Theory of reflectance and emittance spectroscopy, second ed. Cambridge University Press, Cambridge, pp. 528.
Longobardo, A., Palomba, E., Capaccioni, F., Ciarniello, M., Tosi, F., Mottola, S., Moroz, L., Filacchione, G., Raponi, A., Quirico, E., Zinzi, A., Capria, M.T., Bockelee-Morvan, D., Erard, S., Leyrat, C., Rinaldi, G., Dirri, F., 2017a. Photometry as indicator of comets surface roughness. European Planetary Science Congress 2017. Id. EPSC2017-781
Longobardo, A., Palomba, E., Capaccioni, F., De Sanctis, M.C., Tosi, F., Ammannito, E., Schroeder, S.E., Zambon, F., Raymond, C.A., Russell, C.T., 2014. Photometric behavior of spectral parameters in vesta dark and bright regions as inferred by the dawn VIR spectrometer. Icarus 240, 20:35.
Longobardo, A., Palomba, E., De Sanctis, M.C., Ciarniello, M., Galiano, A., Tosi, F., Carrozzo, F.G., Raponi, A., Capria, M.T., Zambon, F., Ammannito, E., Raymond, C.A., Russell, C.T., Rognini, E., 2017b. Photometry of the occator faculae on ceres. European Planetary Science Congress 2017. Id. EPSC2017-782
Lucey, P.G, 1998. Model near-Infrared optical constants of olivine and pyroxene as a function of iron content. J. Geophys. Res. 103, 1703–1713.
McSween Jr., H.Y., Bennett III, M.E., Jarosewich, E., 1991. The mineralogy of ordinary chondrites and implications for asteroid spectrophotometry. Icarus 90, 107–116.
Mikouchi, T., Komatsu, M., Hagiya, K., Oshumi, K., Zolensky, M.E., Hoffman, V., Martinez, J., Hochleitner, R., Kaliwoda, M., Terada, Y., Yagi, N., Takata, M., Satake, W., Aoyagi, Y., Takenouchi, A., Karouji, Y., Uesugi, M., Yada, T., 2014. Mineralogy and cristallography of some Itokawa particles returned by the Hayabusa asteroidal sample return mission. Earth Planets Space 66, 82.
Mukai, T., Araki, H., Mizuno, T., Hatanaka, N., Nakamura, A.M., Kamei, A., Nakayama, H., Cheng, A., 2002. Detection of mass, shape and surface roughness of target asteroid of MUSES-c by LIDAR. Adv. Space Res. 29 (8), 1231–1235.
Mustard, J.F., Pieters, C.M., 1989. Photometric phase functions of common geologic minerals and applications to quantitative analysis of mineral mixture reflectance spectra. J. Geophys. Res. 94, 13619–13634.
Nakamura, T., Nakamura, A.M., Saito, J., Sasaki, S., Nakamura, R., Demura, H., Akiyama, H., Tholen, D., team, A., 2001. Multi-band imaging camera and its sciences for the japanese near-earth asteroid mission MUSES-c. Earth Planets Space 53, 1047–1063.
Nakamura, T., Noguchi, T., Tanaka, M., Zolensky, M.E., Kimura, M., Tsuchiyama, A., Nakata, A., Ogami, T., Ishida, H., Uesugi, M., Yada, T., Shirai, K., Fujimura, A., Okazaki, R., Sandford, S.A., Ishibashi, Y., Abe, M., Okada, T., Ueno, M., Mukai, T., Yoshiwaka, M., Kawaguchi, J., 2011. Itokawa dust particles: a direct link between s-type asteroids and ordinary chondrites. Science 333, 1113.
Ody, A., Poulet, F., Langevin, Y., Bibring, J.P., Bellucci, G., Altieri, F., Gondet, B., Vincendon, M., Carter, J., Manaud, N., 2012. Global maps of anhydrous minerals at the surface of mars from OMEGA/mex. J. Geophys. Res. 117, E00J14.
Okada, T., Kate, M., Fujimura, A., Tsunemi, H., Kitamoto, S., 2000. X-ray fluorescence spectrometer onboard muses-c. Adv. Space Res. 25 (2), 345–348.
Oshtrakh, M., Petrova, E.V., Grokhovsky, V.I., Semionkin, V.A., 2008. A study of ordinary chondrites by Moessbauer spectroscopy with high-velocity resolution. Meteorit. Planet. Sci. 43, 941–958. Nr 5
P., S., 2012. Stooke small bodies maps v2.0. MULTI-SA-MULTI-6-STOOKEMAPS -v2.0. NASA Planetary Data System.
Palomba, E., Longobardo, A., De Sanctis, M.C., Zinzi, A., Ammannito, E., Marchi, S., Tosi, F., Zambon, F., Capria, M.T., Russell, C.T., Raymond, C.A., Cloutis, E.A., 2015. Detection of new olivine-rich locations on vesta. Icarus 258, 120–134.
Poulet, F., Gomez, C., Bibring, J.P., Langevin, Y., Gondet, B., Pinet, P., Bellucci, G., Mustard, J., 2007. Martian surface mineralogy from observatoire pour la mineralogie, l'eau, les glaces et l'activit on board the mars express spacecraft (OMEGA/mex): global mineral maps. J. Geophys. Res. 112.
Roush, T.L., 2005. Near-infrared (0.67-4.7 μm) optical constants estimated for montmorillonite. Icarus 179. 259–254
Saito, J., Miyamoto, H., Nakamura, R., Ishiguro, M., Michikami, T., Nakamura, A.M., Demura, H., Sasaki, S., Hirata, N., Honda, C., Yamamoto, A., Yokota, Y.F., Yoshida, F., tholen, D.J., Gaskell, R.W., Hashimoto, T., Kubota, T., Higuchi, Y., Nakamura, T., Smith, P., Hiraoka, K., Honda, T., Kobayashi, S., Furuya, M., Matsumoto, N., Nemoto, E., Yukishita, A., Kitazato, K., Dermawan, B., Sogame, A., Terazono, J., Shinohara, C., Akiyama, H., 2006. Detailed images of asteroid 25143 Itokawa from Hayabusa. Science 312.
Schroeder, S., Mottola, S., Keller, U., Raymond, C., Russell, C., 2013. Resolved photometry of vesta reveals physical properties of crater regolith. American Astronomical Society, DPS Meeting 45. Id.112.02
Sunshine, J.M., Pieters, C.M., 1993. Estimating modal abundances from the spectra of natural and laboratory pyroxene mixtures using the modified gaussian model. J. Geophys. Res. 98 (E5), 9075–9087.
Tsuchiyama, A., Uesugi, M., Uesugi, K., Nakano, T., Noguchi, R., Matsumoto, T., Matsuno, J., Nagano, T., Imai, Y., Shimada, A., Takeuchi, A., Suzuki, Y., Nakamura, T., Noguchi, T., Takeuchi, A., Suzuki, Y., Nakamura, T., 2014. Three-dimensional microstructure of samples recovered from asteroid 25143 itokawa: comparison with LL5 and LL6 chondrite particles. Meteorit. Planet. Sci. 49, 172–187. Nr 2
Yano, H., Kubota, T., Miyamoto, H., Okada, T., Scheeres, D., Takagi, Y., Yoshida, K., Abe, M., Barnouin-Jha, O., Fujiwara, A., Hasegawa, S., Hashimoto, T., Ishiguro, M., Kato, M., Kawaguchi, J., Mukai, T., Saito, J., Sasaki, S., Yoshiwaka, M., 2006. Touchdown of the Hayabusa spacecraft at the muses sea on Itokawa. Science 312, 1350–1353.
Yurimoto, H., Abe, K., Abe, M., Ebihara, M., Fujimura, A., Hashiguchi, M., Hashizume, K., Ireland, T.R., Itoh, S., Katayama, J., Kato, C., Kawaguchi, J., Kawasaki, N., Kitajima, F., Kobayashi, S., Meike, T., Mukai, T., Nagao, K., Nakamura, T., Naraoka, H., Noguchi, T., Okazaki, R., Park, C., Sakamoto, N., Seto, Y., Takei, M., Tsuchiyama, A., Uesugi, M., Wakaki, S., Yada, T., Yamamoto, K., Yoshiwaka, M., Zolensky, M.E., 2011. Oxygen isotopic composition of asteroidal materials returned from Itokawa by the Hayabusa mission. Science 333, 1116–1119.